




Cite this: *RSC Adv.*, 2018, 8, 396

Cathodoluminescence of $\text{Y}_2\text{O}_3:\text{Ln}^{3+}$ (Ln = Tb, Er and Tm) and $\text{Y}_2\text{O}_3:\text{Bi}^{3+}$ nanocrystalline particles at 200 keV

Daniel den Engelsen,* George R. Fern,* Terry G. Ireland * and Jack Silver*

The cathodoluminescence (CL) spectra of nanocrystalline $\text{Y}_2\text{O}_3:\text{Tb}^{3+}$ (0.3%), $\text{Y}_2\text{O}_3:\text{Er}^{3+}$ (1%), $\text{Y}_2\text{O}_3:\text{Tm}^{3+}$ (2%) and $\text{Y}_2\text{O}_3:\text{Bi}^{3+}$ (1%) were recorded in a transmission electron microscope at 200 keV, low current density and various temperatures. The quenching energy of the intrinsic luminescence of the various $\text{Y}_2\text{O}_3:\text{Ln}^{3+}$ (Ln = Tb, Er and Tm) phosphors was found to be 0.25 eV. The intrinsic luminescence and the strongest spectral transitions of Ln^{3+} in these three phosphors exhibit similar temperature behaviour at temperatures > -50 °C, *viz.* a small increase of the spectral radiance upon increasing the temperature. Increasing the temperature beyond -50 °C led to complete quenching of the intrinsic luminescence at room temperature, whereas the radiance of the Ln^{3+} spectral transitions only decreased slightly. An extended Jablonski diagram for the energy transfer from the self-trapped exciton states in Y_2O_3 to the Ln^{3+} and Bi^{3+} ions is proposed. This diagram also indicates why Tb^{3+} is a better quencher of the intrinsic luminescence in Y_2O_3 than Er^{3+} and Tm^{3+} . The intrinsic luminescence of $\text{Y}_2\text{O}_3:\text{Bi}^{3+}$ largely overlapped with the blue Bi^{3+} emission band, which made an accurate analysis of its temperature behaviour impossible. Nevertheless, we concluded that upon increasing the temperature energy from Bi^{3+} ions at the C_{3i} sites is transferred to Bi^{3+} ions at C_2 sites. From the temperature behaviour of the 539 nm transition of the $^2\text{H}_{11/2} \rightarrow ^4\text{I}_{15/2}$ manifold of $\text{Y}_2\text{O}_3:\text{Er}^{3+}$ the activation energy for this transition could be determined: *viz.* 0.078 eV (623 cm^{-1}).

Received 21st November 2017
 Accepted 15th December 2017

DOI: 10.1039/c7ra12644a

rsc.li/rsc-advances

Introduction

Recently we have published a study on the intrinsic luminescence in cubic Y_2O_3 and $\text{Y}_2\text{O}_3:\text{Eu}^{3+}$ generated in a transmission electron microscope (TEM).¹ The intrinsic luminescence from Y_2O_3 consists of three broad emission bands: the strongest is in the near UV with a centre wavelength (λ_0) at 353 nm ($28\,330\text{ cm}^{-1}$) and two, much weaker, bands manifest at 675 nm ($14\,810\text{ cm}^{-1}$) and 770 nm ($12\,990\text{ cm}^{-1}$).¹ This intrinsic luminescence from Y_2O_3 excited by high energy electrons is rather strong at temperatures < -50 °C and is quenched at room temperature.

The intrinsic luminescence of Y_2O_3 in the near UV has been studied by scientists who hoped to enhance this luminescence for scintillator applications;^{2–9} the weak deep-red intrinsic luminescence bands at 675 nm and 770 nm have not been observed (or described) by other authors. In ref. 1 we also reported the quenching of the intrinsic luminescence by a mechanism other than temperature quenching, *viz.* doping of Y_2O_3 by rare earth ions, such as Nd^{3+} , Eu^{3+} , Tb^{3+} and Tm^{3+} . This had already been observed by Wickersheim and Lefever¹⁰ in 1964

and later by Jacobsohn *et al.*³ and Tanner *et al.*¹¹ Jacobson *et al.* observed a strong reduction of the intrinsic Y_2O_3 luminescence upon doping with Tb^{3+} , while Hayes *et al.*⁷ mentioned weak intrinsic luminescence of Y_2O_3 upon doping with Eu^{3+} . We explained this quenching mechanism in $\text{Y}_2\text{O}_3:\text{Eu}^{3+}$ in terms of radiationless energy transfer from self-trapped excitons (STEs) in the Y_2O_3 lattice to the $^5\text{D}_4$ level of the Eu^{3+} ion in the Y_2O_3 lattice.¹ Radiationless energy transfer in phosphors may be considered as an example of resonance energy transfer described by Förster in 1948 (FRET).¹² According to this theory the efficiency of radiationless energy transfer depends on the spectral overlap integral between a donor and acceptor state. Based on the theory of resonance energy transfer it is to be expected that there must be differences in the energy transfer from the excited intrinsic energy level of Y_2O_3 (donor state) to various rare earth dopants (acceptors). With this idea in mind we started an investigation of the intrinsic luminescence in $\text{Y}_2\text{O}_3:\text{Tb}^{3+}$ (0.3%), $\text{Y}_2\text{O}_3:\text{Er}^{3+}$ (1%), $\text{Y}_2\text{O}_3:\text{Tm}^{3+}$ (2%) and $\text{Y}_2\text{O}_3:\text{Bi}^{3+}$ (1%) by high energy cathodoluminescence (CL) in a TEM.

Experimental

Materials and synthesis

Yttrium oxide (99.99%, Ampere Industrie, France) and terbium(III) oxide (99.99%, Neo Performance Materials, UK), erbium

Centre for Phosphor and Display Materials, Wolfson Centre for Materials Processing, Brunel University London, Uxbridge, Middlesex, UB8 3PH, UK. E-mail: jack.silver@brunel.ac.uk



oxide (99.99%, Neo Performance Materials, UK), thulium oxide (99.99%, Neo Performance Materials, UK) and bismuth(III) oxide (99.99%, Neo Performance Materials, UK) were used to prepare the lanthanide, bismuth and yttrium nitrate stock solutions. Urea, nitric acid, oxalic acid and isopropanol (Fisher Scientific, UK) were used for the syntheses. All chemicals were used as received. The general technique for controlled homogeneous precipitation of spherical monosized submicrometre rare earth oxide precursor particles, namely, the hydroxycarbonates, is by a single nucleation event, followed by uniform growth of nuclei. This is achieved using the slow aqueous thermal decomposition of urea where the reactants are added very slowly, deterring localised excess of reagent that would produce many nuclei and small particles that would form a floc. Thus, homogeneous precipitation is a technique that allows the slow addition of reactant, deterring localised excess of reagent, it is based on the slow hydrolysis of (or some other reaction) a solute, yielding a product that reacts to form a desired precipitate. When the above requirement is met hydrolysis will proceed uniformly throughout the solution, at a rate that is also, dependent on temperature. Precipitation will be slow, nucleation followed by particle growth will remove the reacting ions as they are produced inhibiting any further nucleation, formation of the particles being controlled by the concentration of reactants.

The synthesis of spherical monosized submicrometre rare earth oxide precursor particles of $Y_2O_3:Ln^{3+}$ and $Y_2O_3:Bi^{3+}$ were prepared by the following method.

The oxides of the desired rare earth elements were digested in dilute nitric acid to form nitrate stock solutions (0.25 M) within a pH range of 1 to 3. To synthesise for example $Y_2O_3:Bi^{3+}$ ($Bi = 2.0$ mol%) $Y(NO_3)_3$ (24.5 ml), $Bi(NO_3)_3$ (0.5 ml) and deionised water, (475 ml) were added to a one litre beaker and heated to boiling (this temperature was maintained throughout the reaction) at this point urea (15.01 g) was added. When turbidity was observed the solution was aged for one hour. The solution was then filtered whilst still hot (cooling could allow the uncontrolled nucleation of any residual reactants to form which would affect the monodispersity of the resulting hydroxycarbonate phosphor precursor particles). The precipitate was then washed three times with deionised water (100 ml), then dried in an oven at 80 °C for 8 hours. The precursor particles were then annealed in an alumina crucible in air at 980 °C 6 hours resulting in cubic spherical submicrometre $Y_2O_3:Bi^{3+}$ phosphor particles.

The above method produces approximately 1.7 g of phosphor powder the precipitation method is scalable up to ten times of the example described above.

X-ray powder diffraction

The crystallinity of the prepared $Y_2O_3:Tb^{3+}$ (0.3%), $Y_2O_3:Er^{3+}$ (1%), $Y_2O_3:Tm^{3+}$ (2%) and $Y_2O_3:Bi^{3+}$ (1%) materials was checked by X-ray powder diffraction (XRPD) using a Bruker D8 Advance X-ray powder diffractometer fitted with a nickel-filtered copper source and a LynxEye silicon strip detector. The analysis of the XRPD spectra has also been described in our previous work.^{1,13–16} These XRD analyses confirmed that our powder

samples had the cubic bixbyite structure of Y_2O_3 . The dopant concentration of the lanthanide ions or Bi^{3+} in Y_2O_3 was not separately checked.

Transmission electron microscope

The submicron spherical $Y_2O_3:Ln^{3+}$ and $Y_2O_3:Bi^{3+}$ samples were investigated with a TEM (2100F, JEOL, Japan) equipped with a Schottky-type field emission gun. The TEM was equipped with a Vulcan CL detector, Gatan, USA, for imaging and spectroscopic purposes. This system used a Czerny–Turner spectrometer with back-illuminated CCD and gratings with 1200 or 2400 grooves per mm for collection of CL emission spectra. Light was collected from the sample using a mirror above and below the sample, which enabled a solid angle of about 5 sr, which is almost half of a sphere. This high solid angle made light collection highly efficient and enabled the collection of CL at low intensity. Unfortunately, the cooled detector of this spectrometer did not allow the recording of spectra at $\lambda < 400$ nm. A small cryostat connected to the sample holder enabled cooling of the samples in the TEM down to 102 K (171 °C); adjustment of the sample temperature anywhere between 102 K and 303 K was facile.

CL-spectra were recorded with a focussed e-beam, spot size 1.5 nm, and defocussed e-beam, spot size ~ 5 μ m. The latter method was preferred, because the lower current density (about 7 orders of magnitude lower) had as consequence that specimen degradation due to the electron bombardment was avoided. Degradation due to the e-beam is easy to observe with phosphor specimens, because in that case the CL decreases as function of time due to lattice damage. This damage is due to the formation of defects or even recrystallization in the case of a focussed e-beam with a very small spot size. For $Y_2O_3:Er^{3+}$ we have observed a CL decrease with a focussed e-beam of about 10% during 1 minute. In order to get sufficient luminescence with a defocussed e-beam, the specimens had to be thicker than 200 nm, preferably >1 μ m, and the area from which the luminescence was collected must be larger than 1 μ m as well. Thus, a rather large area of the sample was excited which impeded the collection of CL-spectra from individual nano-sized particles (using a focussed e-beam). For the CL-measurements in the TEM copper grids coated with thin carbon films having small holes (holey carbon films) were used as substrates.

Results

Microscope images

Fig. 1 and 2 present TEM images of the materials described in this report.

Fig. 1 shows that the $Y_2O_3:Tm^{3+}$ and $Y_2O_3:Er^{3+}$ particles are spherical and have diameters of about 150 nm and 250 nm respectively. These spheres consist of crystallites, which are about 30 nm. The $Y_2O_3:Tb^{3+}$ particles have more crystalline shapes and are smaller than 100 nm. Fig. 1c and d are scanning transmission electron microscope (STEM) images of $Y_2O_3:1\%$ Er^{3+} : Fig. 1c is a high-angle annular dark-field (HAADF) image, while Fig. 1d is an image of the panchromatic luminescence.



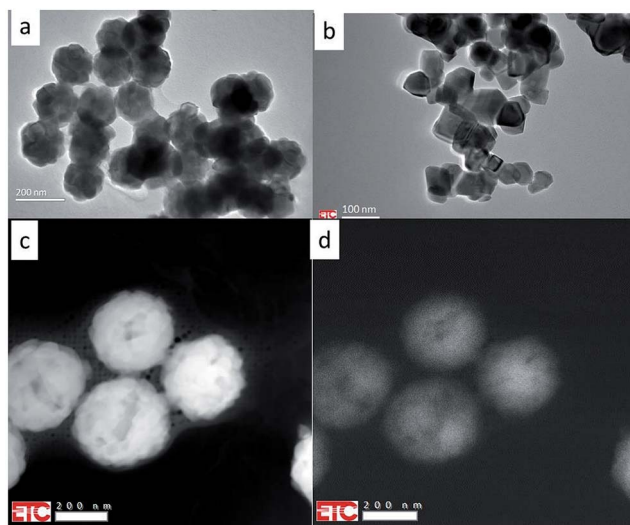


Fig. 1 TEM images of $\text{Y}_2\text{O}_3:\text{Ln}^{3+}$ at e-beam voltage of 200 kV. (a) $\text{Y}_2\text{O}_3:2\% \text{Tm}^{3+}$; (b) $\text{Y}_2\text{O}_3:0.3\% \text{Tb}^{3+}$; (c) $\text{Y}_2\text{O}_3:1\% \text{Er}^{3+}$ (high-angle annular dark-field image (HAADF)); (d) panchromatic luminescence image of $\text{Y}_2\text{O}_3:1\% \text{Er}^{3+}$ (same area as shown in (c)).

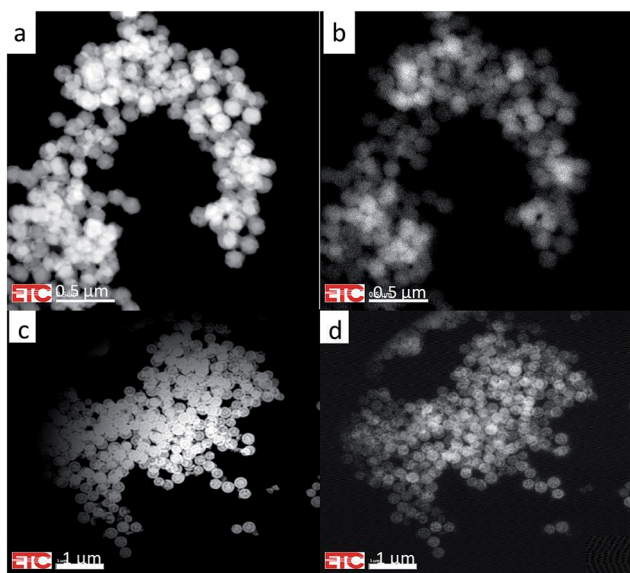


Fig. 2 (a) HAADF image of $\text{Y}_2\text{O}_3:\text{Tm}^{3+}$ spherical particles at 200 kV and 25 °C. (b) Panchromatic luminescence image of same area as shown in (a). (c) HAADF image of $\text{Y}_2\text{O}_3:\text{Bi}^{3+}$ spherical particles at 200 kV and 31.2 °C. (d) Panchromatic luminescence image of same area as shown in (c).

This luminescence originates mainly from the green $\text{Er}^{3+} 4\text{S}_{3/2} \rightarrow 4\text{I}_{15/2}$ multiplet. The scanning speed was adjusted to suppress smearing out of the image.

Fig. 2 shows STEM images of clusters of spherical $\text{Y}_2\text{O}_3:\text{Tm}^{3+}$ and $\text{Y}_2\text{O}_3:\text{Bi}^{3+}$ particles: Fig. 2a and c are HAADF images, while Fig. 2b and d are images of the panchromatic luminescence from the same cluster of particles shown in Fig. 2a and c respectively. For maximizing the CL of the samples, locations were selected on the holey-carbon-Cu-grids with some

agglomeration of spheres to obtain sufficient thickness. Fig. 2 manifests typical examples of these locations. The CL-spectra recorded of $\text{Y}_2\text{O}_3:\text{Bi}^{3+}$ refer to the cluster presented in Fig. 2c and d.

The luminescence that creates the panchromatic image of Fig. 2b is mainly from the blue emission from Tm^{3+} (the $1\text{D}_2 \rightarrow 3\text{F}_4$ multiplet), while that of Fig. 2d is from the blue and green emission bands of Bi^{3+} , to be described hereafter.

The images of the panchromatic luminescence of the $\text{Y}_2\text{O}_3:1\% \text{Er}^{3+}$ and $\text{Y}_2\text{O}_3:2\% \text{Tm}^{3+}$ particles in Fig. 1d and 2b respectively are evidence for uniform Er^{3+} and Tm^{3+} doping in both one particle and all the particles: this is a vindication of the synthetic procedure. The non-uniformity seen in the particles in Fig. 1d refers to the boundaries of crystallites, which can also be observed in Fig. 1c. As mentioned in the previous section, thickness of the phosphor particles is an important parameter in homogeneous materials: the luminance increases as the thickness increases. This also refers to the present TEM study, in which the penetration depth of the impinging electrons is more than two orders of magnitude larger than the diameter of the particles. Particles on top of others yield more luminescence: this is clearly illustrated in Fig. 2. The luminance effect of thickness differences between the centre of a spherical particle and the edge can also be observed in Fig. 1d. However, the uniformity of the luminescence in Fig. 2d of $\text{Y}_2\text{O}_3:1\% \text{Bi}^{3+}$ is less convincing, because some particles show edges with slightly enhanced luminance. In a recent study on the panchromatic luminescence from phosphor particles in a scanning electron microscope (SEM) we have attributed the enhanced edge luminance to backscattered electrons from particles that are mainly situated below the actual particle.¹⁷ In a TEM the backscatter coefficient is much lower than in a SEM due to the high beam voltage; as a consequence, an enrichment of Bi^{3+} at the surface of the $\text{Y}_2\text{O}_3:\text{Bi}^{3+}$ particles represented in Fig. 2d cannot be excluded.

Cathodoluminescence spectra

The CL-spectra of $\text{Y}_2\text{O}_3:\text{Tb}^{3+}$ (0.3%), $\text{Y}_2\text{O}_3:\text{Er}^{3+}$ (1%), $\text{Y}_2\text{O}_3:\text{Tm}^{3+}$ (2%) and $\text{Y}_2\text{O}_3:\text{Bi}^{3+}$ (1%) were recorded at 200 keV between -170 °C and $+30$ °C, usually in steps of 25 °C. In most cases a defocussed e-beam was used (TEM-mode) with a current density at the sample of $\sim 0.05 \text{ A cm}^{-2}$. Fig. 3–5 present the CL spectra of $\text{Y}_2\text{O}_3:\text{Tb}^{3+}$ (0.3% and 1%), $\text{Y}_2\text{O}_3:\text{Er}^{3+}$ (1%) and $\text{Y}_2\text{O}_3:\text{Tm}^{3+}$ (2%) respectively. In these figures only the spectra recorded at the minimum and/or minimum and maximum temperatures are shown for clarity reasons.

The intrinsic luminescence of $\text{Y}_2\text{O}_3:0.3\% \text{Tb}^{3+}$ in Fig. 3 can be observed between 400 nm and 470 nm, whereas $\text{Y}_2\text{O}_3:1\% \text{Tb}^{3+}$ did not yield any intrinsic luminescence at this temperature. At room temperature the intrinsic luminescence in $\text{Y}_2\text{O}_3:0.3\% \text{Tb}^{3+}$ disappeared completely. As mentioned above, we could not detect the UV-part of the intrinsic luminescence of Y_2O_3 . We measured λ_0 , the wavelength at the maximum, of the intrinsic luminescence of Y_2O_3 at 353 nm;¹ however, this peak wavelength was also measured at other wavelengths by other scientists, see for instance Table 1 in ref. 1. By excitation of Y_2O_3 with X-rays Jacobsohn *et al.*³ measured 410 nm; by doping Y_2O_3



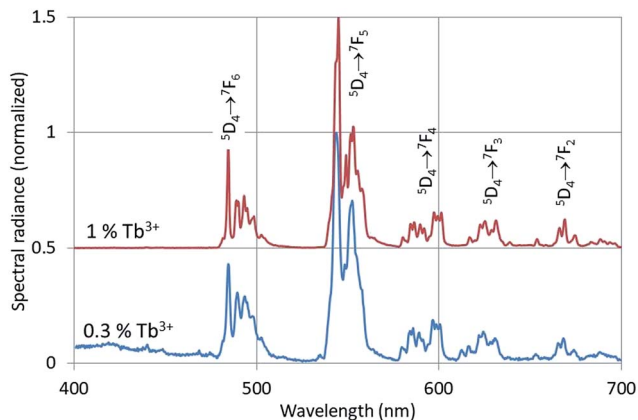


Fig. 3 CL-spectra of $\text{Y}_2\text{O}_3:\text{Tb}^{3+}$ with 0.3% Tb^{3+} and 1% Tb^{3+} at -169°C . The spectra were recorded with defocussed e-beam (TEM-mode). Bandpass for $\text{Y}_2\text{O}_3:0.3\% \text{Tb}^{3+}$ was 2 nm, bandpass for $\text{Y}_2\text{O}_3:1\% \text{Tb}^{3+}$ was 1 nm. The spectrum for the 1% Tb^{3+} sample has been shifted vertically.

Table 1 Effect of current density on the intensity ratio in $\text{Y}_2\text{O}_3:\text{Tb}^{3+}$ and $\text{Y}_2\text{O}_3:\text{Er}^{3+}$ at -170°C

	Focussed	Defocussed
$\text{Y}_2\text{O}_3:\text{Tb}^{3+}$: SR543/SR412 ^a	3.1	12.7
$\text{Y}_2\text{O}_3:\text{Er}^{3+}$: SR564/SR412	14.2	52

^a SR_i is the spectral radiance (intensity) of the luminescence at *i* nm. At 543 nm and 564 nm are the main peaks of $\text{Y}_2\text{O}_3:\text{Tb}^{3+}$ and $\text{Y}_2\text{O}_3:\text{Er}^{3+}$ respectively.

with 20 ppm Tb^{3+} they found that the peak wavelength moved to about 360 nm. The Tb^{3+} transitions in Fig. 3 have been assigned according to the published energy levels of Tb^{3+} in Y_2O_3 .¹⁸ As we have indicated in our study on the intrinsic luminescence in undoped Y_2O_3 and $\text{Y}_2\text{O}_3:\text{Eu}^{3+}$, the spectral radiance between 400 nm and 420 nm may be used to analyse the temperature behaviour of the intrinsic luminescence.

In Fig. 4 the intrinsic luminescence of Y_2O_3 can also be observed in the low temperature spectrum of $\text{Y}_2\text{O}_3:\text{Er}^{3+}$ between 400 nm and 460 nm; this spectrum also shows intrinsic deep-

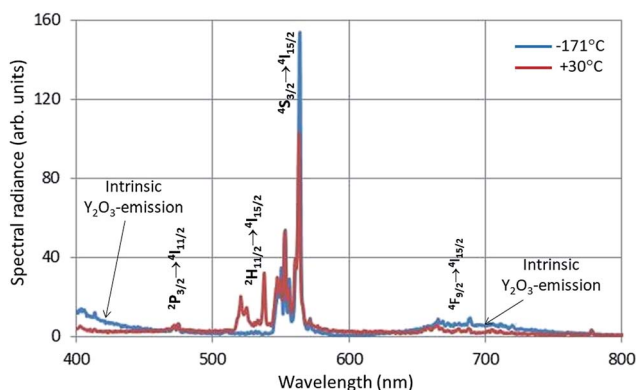


Fig. 4 CL-spectra of $\text{Y}_2\text{O}_3:1\% \text{Er}^{3+}$ at -171°C and 30°C . Spectra recorded with a stationary focussed e-beam (STEM-mode).

red luminescence at about 675 nm. The peak wavelength of this deep-red luminescence cannot be determined exactly because of the ${}^4\text{F}_{9/2} \rightarrow {}^4\text{I}_{15/2}$ transition manifold. The reason that we can observe this deep-red intrinsic luminescence in $\text{Y}_2\text{O}_3:\text{Er}^{3+}$ is probably the high current density of the focussed e-beam.

The Er^{3+} transitions in Fig. 4 have been assigned according to the published energy levels of Er^{3+} in Y_2O_3 .¹⁹ As mentioned before, the stationary e-beam used to record the spectra presented in Fig. 4 caused some degradation of the sample. The analyses of the spectral data, to be presented hereafter, are based on data from a defocussed beam without e-beam degradation.

For $\text{Y}_2\text{O}_3:\text{Tb}^{3+}$ and $\text{Y}_2\text{O}_3:\text{Er}^{3+}$ CL spectra were recorded both with a focussed and with a defocussed e-beam. With a focussed, stationary e-beam the intrinsic luminescence became more intense compared to the Ln^{3+} luminescence, as presented in Table 1.

A very high current density of the e-beam is thus beneficial for the intrinsic luminescence; however, it is detrimental for the sample when long exposures are necessary. In ref. 1 we have shown that the radiance (integrated intensity) of the intrinsic luminescence is much larger than the radiance of the strongest Eu^{3+} peak: hence, from an energy point of view, Table 1 is misleading.

The CL-spectrum of $\text{Y}_2\text{O}_3:2\% \text{Tm}^{3+}$ at -165°C also shows intrinsic luminescence between 400 nm and about 450 nm. The Tm^{3+} transitions in Fig. 5 have been assigned according to the published energy levels of Tm^{3+} in Y_2O_3 .¹⁸ The deep-red intrinsic luminescence at about 675 nm cannot be clearly observed due to the ${}^1\text{G}_4 \rightarrow {}^3\text{F}_4$ transition manifold of Tm^{3+} . The radio-luminescence spectrum of $\text{Y}_2\text{O}_3:0.15\% \text{Tm}^{3+}$ was measured by Fujimoto *et al.*⁹ by excitation with 5.5 MeV- α -rays. They measured 360 nm for λ_0 of the UV-intrinsic luminescence; they also reported another (smaller) emission band at about 460 nm, which must be attributed to the ${}^1\text{D}_2 \rightarrow {}^3\text{F}_4$ Tm^{3+} multiplet.

Fig. 6 shows the CL-spectra of $\text{Y}_2\text{O}_3:1\% \text{Bi}^{3+}$ recorded at 200 kV and various temperatures.

Fig. 6 shows three broad emission bands: p1 is the deep-red intrinsic emission of Y_2O_3 , p2 and p3 are the green and blue

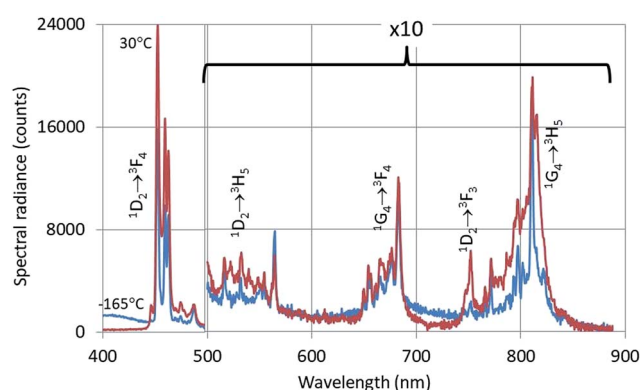


Fig. 5 CL-spectra of $\text{Y}_2\text{O}_3:2\% \text{Tm}^{3+}$ at -165°C and 30°C . Spectra recorded with a defocussed e-beam (TEM-mode). Bandpass: 2 nm.



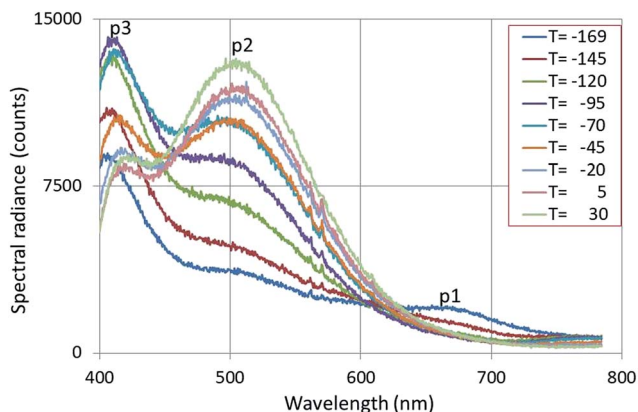


Fig. 6 CL-spectra of $\text{Y}_2\text{O}_3:1\% \text{Bi}^{3+}$ recorded at 200 kV and various temperatures, indicated in degrees C. The emission bands p1, p2 and p3 are explained in the text.

emission bands of $\text{Y}_2\text{O}_3:\text{Bi}^{3+}$ respectively.^{20,21} The spectra presented in Fig. 6 will be analysed by deconvolution hereafter. The λ_0 of the green band p2 was found (after deconvolution) to be at 504 nm, which deviates considerably from 477 nm as reported by Jafer *et al.*²¹ by CL. Herein the λ_0 of the blue band was found to be at 417 nm, which is close to 413 nm, reported by Jafer *et al.*²¹

Analysis of the spectra

In this section we shall describe the temperature behaviour of the intrinsic luminescence of $\text{Y}_2\text{O}_3:\text{Ln}^{3+}$ and $\text{Y}_2\text{O}_3:\text{Bi}^{3+}$ phosphors in terms of Arrhenius plots. Fig. 7 is a typical example of the intrinsic luminescence in $\text{Y}_2\text{O}_3:\text{Er}^{3+}$.

Since we could not measure the complete intrinsic luminescence band in the near UV with λ_0 at 353 nm, the radiance (integrated intensity) of the intrinsic emission could not be evaluated. In analysing the intrinsic luminescence in Y_2O_3 and $\text{Y}_2\text{O}_3:\text{Eu}^{3+}$,¹ we found that identical results were obtained by using the spectral radiance at the top, SR353, and at some point

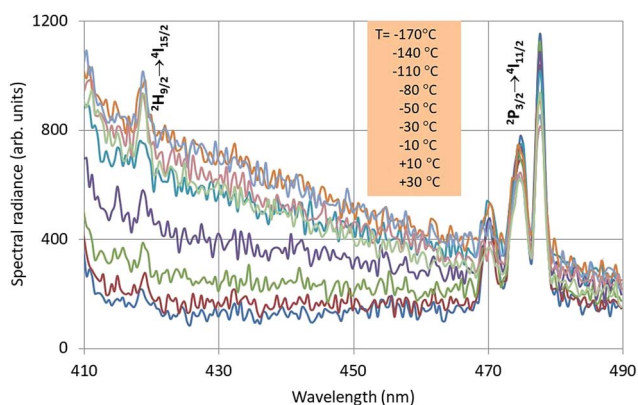


Fig. 7 Intrinsic luminescence in $\text{Y}_2\text{O}_3:\text{Er}^{3+}$ measured at 200 kV with defocused e-beam and bandpass at 2 nm. The insert shows the sequence of the temperature. Two Er^{3+} transition manifolds can be observed.

at the flank of the intrinsic luminescence band, say SR412. This means that the full width at half maximum (FWHM) does not change upon varying the temperature. For the analyses we shall use the spectral radiance of the intrinsic luminescence at 412 nm, SR412, assuming that the intrinsic luminescence of $\text{Y}_2\text{O}_3:\text{Tb}^{3+}$, $\text{Y}_2\text{O}_3:\text{Er}^{3+}$ and $\text{Y}_2\text{O}_3:\text{Tm}^{3+}$ all behaves identical to the luminescence in $\text{Y}_2\text{O}_3:\text{Eu}^{3+}$. The selection of 412 nm is also based on the requirement to be sufficiently far from any interfering Ln^{3+} transition.

Fig. 8 is the Arrhenius plot of SR412 and SR551 of $\text{Y}_2\text{O}_3:0.3\% \text{Tb}^{3+}$.

The peak at 551 nm is not the strongest transition of the $^5\text{D}_4 \rightarrow ^7\text{F}_5$ multiplet as can be seen in Fig. 3. The 551 nm peak originates from cation sites with C_2 symmetry, whereas the transition at 543 nm is a doublet consisting of peaks originating from cation sites with C_2 and cation sites with C_{3i} symmetry.^{22,23} Since the temperature behaviours of the C_2 and C_{3i} transitions are different due to energy transfer from the C_{3i} states to the C_2 states, SR551 is a better choice for the present analysis. As mentioned above, radiance (integrated intensity) is the preferred quantity to describe temperature behaviour. We have checked the temperature variation of the radiance of the 551 nm peak (by deconvolution using Lorentzian profiles) with the variation of SR551 (intensity at the maximum): these were identical. The reason is that the CL-spectra have been recorded with a rather large bandpass of 2 nm: the FWHM of the spectral transitions is then largely determined by the monochromator and thus (almost) equal for the various temperatures.

Fig. 8 presents that the temperature behaviour of the intrinsic luminescence represented by SR412 has a low temperature region, where the spectral radiance (SR) increases a little bit upon increasing the temperature, while in the high temperature region SR decreases strongly. This behaviour of SR can be represented by the following equation:

$$\text{SR}(T) = \frac{C e^{-E_u/kT}}{1 + B e^{-E_q/kT}}, \quad (1)$$

where $\text{SR}(T)$ is the spectral radiance, C is a pre-exponential factor, E_u is the activation energy of the transition, B is the

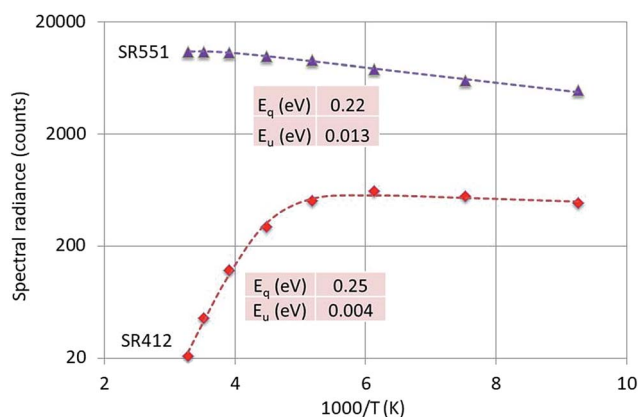


Fig. 8 Arrhenius plot of SR412 and SR551 of $\text{Y}_2\text{O}_3:0.3\% \text{Tb}^{3+}$. Dashed curves are according to eqn (1), fitted to the experimental points. Only the calculated activation energies are indicated.



frequency factor describing thermal quenching in a single barrier model^{24,25} and E_q is the quenching energy; furthermore, k is Boltzmann's constant and T is the absolute temperature. The parameters C , E_u , B and E_q were fitted to the experimental data points with a least squares algorithm. We have recently proposed eqn (1) to describe the temperature behaviour of the laser-activated luminescence in $Y_2O_3:Er^{3+}$.²⁶ The numerator in eqn (1) is the Boltzmann factor that describes the increase of the spectral radiance upon increasing the temperature in the low temperature region (>50 °C). The denominator describes the quenching of the luminescence at high temperature: if $E_u = 0$, then eqn (1) reduces to the Fermi–Dirac equation.^{25,26} In analysing the temperature behaviour of the intrinsic luminescence of Y_2O_3 and $Y_2O_3:Eu^{3+}$,¹ we used the Fermi–Dirac equation ($E_u = 0$), because the increase of the radiance at low temperature was not detected with the focussed e-beam due to (some) beam degradation. Fig. 9 and 10 are Arrhenius plots of the relevant SRs of $Y_2O_3:Er^{3+}$ and $Y_2O_3:Tm^{3+}$ respectively.

The 564 nm peak is the strongest transition of the $^4S_{3/2} \rightarrow ^4I_{15/2}$ manifold in $Y_2O_3:Er^{3+}$ and the 564 nm peak itself

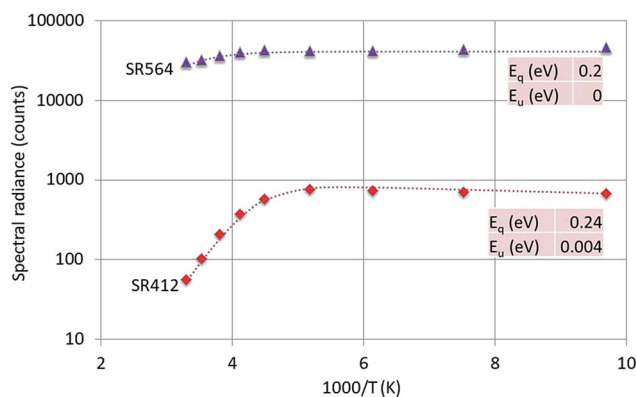


Fig. 9 Arrhenius plot of SR412 and SR564 of $Y_2O_3:1\% Er^{3+}$. Dashed curves are according to eqn (1), fitted to the experimental points. Only the fitted activation energies are indicated.

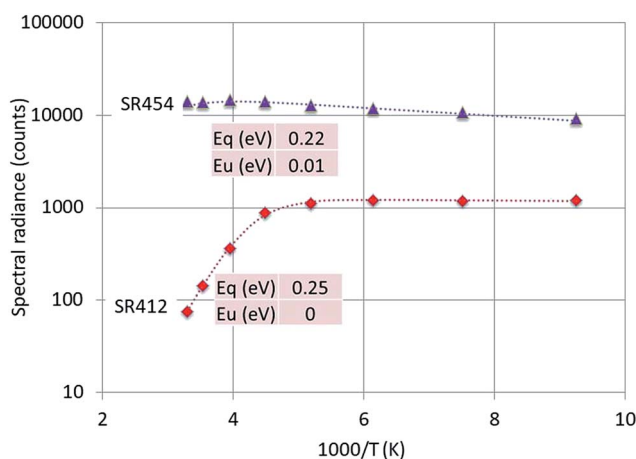


Fig. 10 Arrhenius plot of SR412 and SR454 of $Y_2O_3:2\% Tm^{3+}$. Dashed curves are according to eqn (1), fitted to the experimental points. Only the fitted activation energies are indicated.

is at least a doublet. If this peak has a contribution from a C_{3i} transition, then this could explain the flat behaviour ($E_u = 0$) of SR564 at temperatures < -70 °C.

The luminescence peak at 454 nm is the strongest of the $^1D_2 \rightarrow ^3F_4$ manifold in the CL spectra of $Y_2O_3:Tm^{3+}$ as depicted in Fig. 5. This peak consists of at least 4 transitions as indicated in the laser-activated high-resolution spectrum of $Y_2O_3:Tm^{3+}$ described by Silver *et al.*²⁷ it is therefore obvious to assume that the C_{3i} character of this CL-peak will be modest.

The graphs depicted in Fig. 8–10 show rather similar behaviour: slight increase of SR in the low temperature region upon increasing the temperature and quenching of the intrinsic luminescence at high temperatures. The quenching energy E_q for the intrinsic luminescence is about 0.25 eV for $Y_2O_3:Tb^{3+}$, $Y_2O_3:Er^{3+}$ and $Y_2O_3:Tm^{3+}$, which is larger than E_q (0.14 eV) determined for $Y_2O_3:Eu^{3+}$.¹ We assume that $E_q = 0.14$ eV for $Y_2O_3:Eu^{3+}$ is an underestimate, based on our new measuring technique with a defocussed e-beam in the TEM (which avoids beam degradation of the sample). The quenching energies E_q for the Ln^{3+} spectral peaks represented in Fig. 8–10 are also similar. It should be mentioned that the spread in E_q for these Ln^{3+} transitions is considerable, because the range of experimental values for these SRs is much smaller than one decade.

200 keV-cathodoluminescence in $Y_2O_3:Bi^{3+}$

Fig. 11 shows the deconvolutions of the CL-spectra of $Y_2O_3:Bi^{3+}$ at -120 °C and -20 °C. These spectra can be fitted well with 4 Gaussian profiles with a cm^{-1} base.

The profiles p1, p2 and p3 were already defined in Fig. 6 and p4 is the UV-intrinsic luminescence, of which only the part in the visible ($\lambda > 400$ nm) could be measured. The FWHM and λ_0 for p1 and p4 were taken from ref. 1 for these deconvolutions, while the amplitudes of p1 and p4 were fitted together with the in total 6 Gaussian parameters for p2 and p3. From the deconvoluted spectrum the radiances R_i of the profiles p2, p3 and p4 can be calculated by integration according to:

$$R_i = \int_0^{\infty} SR_i(\nu) d\nu, \quad (2)$$

where SR_i is the spectral radiance for profile i ($i = p2, p3$ or $p4$). The deep-red luminescence band at 675 nm, p1, could not be determined accurately and will be ignored here. The parameter ν indicates frequency in cm^{-1} .

Fig. 12 is the Arrhenius plot of the radiances of p2, p3 and p4, which are the green band of $Y_2O_3:Bi^{3+}$, the blue band and the intrinsic luminescence band respectively.

It should be stressed that the representation of the radiance of the intrinsic luminescence, p4, is not very accurate, because we could not measure at $\lambda < 400$ nm.

Significant in Fig. 12 is the deviation of parallelism of the p2 and p3 curves at temperatures > -70 °C. At higher temperatures the blue band decreases significantly, while the green band still grows. The blue emission band has been attributed to the $^3E_u \rightarrow ^1A_g$ (C_{3i}) transition by Jafer *et al.*,²¹ while these authors attributed the green band to the $^3B \rightarrow ^1A$ (C_2) transition. With this assignment in mind, it is tempting to assume that the kink



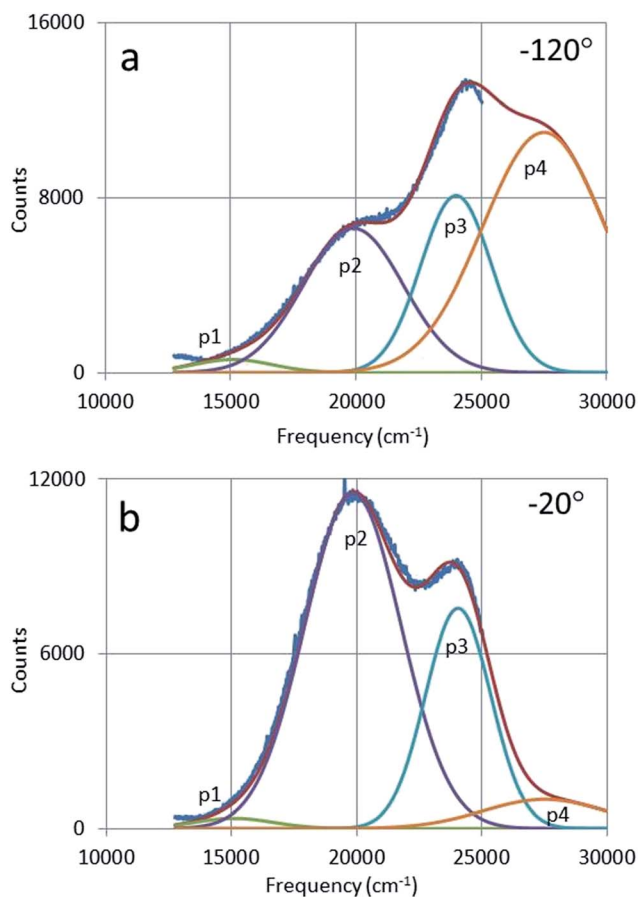


Fig. 11 Deconvolution of CL-spectrum of $\text{Y}_2\text{O}_3:1\% \text{Bi}^{3+}$ at -120°C (a) and -20°C (b) with four Gaussian profiles: p1 and p4 are the intrinsic luminescence bands of Y_2O_3 , while p2 and p3 are the green and blue emission bands respectively of $\text{Y}_2\text{O}_3:1\% \text{Bi}^{3+}$.

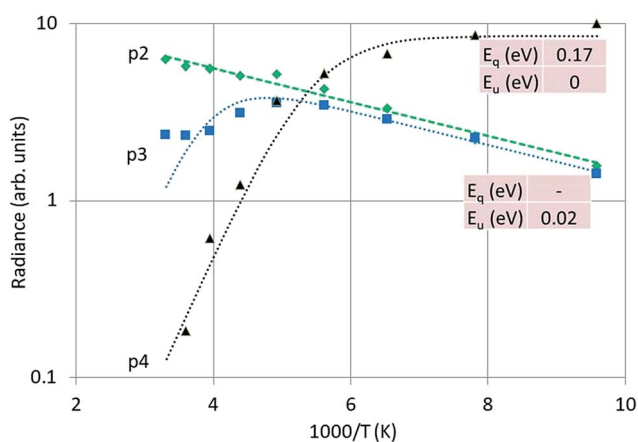


Fig. 12 Arrhenius plot of the green emission band (p2), the blue emission band (p3) and the UV intrinsic luminescence (p4) of $\text{Y}_2\text{O}_3:\text{Bi}^{3+}$. Dashed and dotted curves were fitted with eqn (1) to the experimental points, using radiance instead of spectral radiance.

in the curve for the blue band in Fig. 12 is due to energy transfer from Bi^{3+} at a C_{3i} cation position to Bi^{3+} at a C_2 position. This energy transfer is dependent on the distance between the two

Bi^{3+} ions and should be much less at low Bi^{3+} concentrations. This was not tested in the present study.

Energy transfer in $\text{Y}_2\text{O}_3:\text{Ln}^{3+}$ and $\text{Y}_2\text{O}_3:\text{Bi}^{3+}$

In this section we shall discuss the results that are presented in the preceding sections. In doing so we shall make use of an extended Jablonski diagram that visualizes the energy flows in the phosphors. Hayes *et al.*⁷ concluded from the optical detection of magnetic resonance that the intrinsic luminescence in Y_2O_3 originates from a triplet state. This conclusion poses a difficulty in constructing a Jablonski-type diagram of the energy flows, because radiation from a triplet state is usually slow (phosphorescence), whereas the decay time of the intrinsic luminescence in Y_2O_3 is rather short, between 15 and 200 ns.^{28,29} It should be mentioned that these decay times were determined at room temperature: at low temperature decay times are usually substantially longer.

Fig. 13 is the extended Jablonski diagram of the energy flows in $\text{Y}_2\text{O}_3:\text{Ln}^{3+}$ and $\text{Y}_2\text{O}_3:\text{Bi}^{3+}$ upon bombardment with high energy electron. This diagram is speculative: it needs further confirmation by future work.

The construction of the energy diagram in Fig. 13 is based on the assumption that Y_2O_3 has three levels for the self-trapped exciton (STE), indicated by STE-T, STE-S and STE-Q. STE-T refers to a triplet state, STE-S refers to a singlet state and STE-Q indicates the level of the quenching state, where the inter-system crossing starts. In fact we need four STE-levels; however, to keep the diagram as simple as possible, we ignore here the deep-red intrinsic luminescence. When after being hit by high energy electrons, the almost thermalized electron-hole pairs in the lattice are trapped at STE-T, which is indicated by arrow 1. By phonon interactions the excitons can be promoted to STE-S (arrow 2) and at higher temperature to STE-Q (arrow 3). The

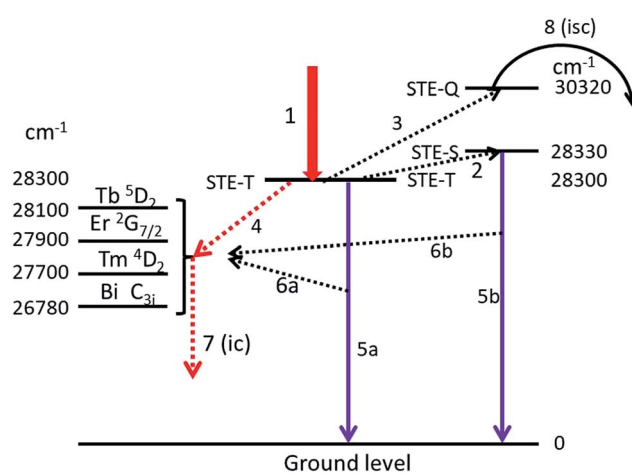


Fig. 13 Jablonski-type diagram visualizing the energy flows in $\text{Y}_2\text{O}_3:\text{Ln}^{3+}$ and $\text{Y}_2\text{O}_3:\text{Bi}^{3+}$ upon e-beam excitation. Left hand side: relevant energy levels in $\text{Y}_2\text{O}_3:\text{Ln}^{3+}$ and $\text{Y}_2\text{O}_3:\text{Bi}^{3+}$, the STE-T (triplet) level of Y_2O_3 has been positioned in the centre and at the right hand side are the STE-S (singlet) and STE-Q (quenching) levels. Arrows are explained in the text. N.B. the energy scale has been distorted for clarity reasons.



location of the energy levels is indicated in cm^{-1} , the levels for STE-T and STE-Q are derived from the Arrhenius plots in Fig. 8–10 and from ref. 1 for positioning STE-S (λ_0 is 353 nm). The separation between STE-T and STE-S is only 0.004 eV (30 cm^{-1}); at $-170 \text{ }^\circ\text{C}$ the population density of STE-S is already over 50% of the population density of STE-T. We assume that energy can be transferred from the STE states of Y_2O_3 to excited states in Ln^{3+} and Bi^{3+} via three different mechanisms:

- (1) From STE-T by radiationless transfer according to Förster's resonance energy transfer (FRET), indicated by arrow 4, to Ln^{3+} and to Bi^{3+} ;
- (2) Via absorption of intrinsic luminescence, indicated by arrows 6a and 6b to Ln^{3+} and to Bi^{3+} ;
- (3) From STE-Q by intersystem crossing, indicated by arrow 8.

The first two energy transfer mechanisms are dominant at low temperatures; the third is leading at high temperatures. When excitons arrive at STE-Q due to phonon interaction at high temperature, they can radiationless transfer energy to the dopants via intersystem crossing. This process will eventually empty the STE-T and STE-S states and at sufficiently high temperature, the intrinsic luminescence will be quenched completely. In the following we shall focus on the first two energy transfer mechanisms.

Arrows 5a and 5b represent the UV intrinsic luminescence. These two arrows indicate the complicated nature of the intrinsic luminescence, which shows fast and slow contributions to the decay.^{28,29} The slow decay component ($>100 \text{ ns}$) is represented by arrow 5a (from STE-T), while the fast component from STE-S is represented by arrow 5b. Arrow 5b explains why the intrinsic luminescence increases slightly upon increasing the temperature from $-170 \text{ }^\circ\text{C}$ to about $-70 \text{ }^\circ\text{C}$, while arrow 5a explains why there is still intrinsic luminescence in Y_2O_3 at about 1 K. The intrinsic luminescence at this very low temperature is supposed to be slow (triplet state). Unfortunately, we could not find literature data to verify this idea.

In order to understand why the Ln^{3+} and Bi^{3+} transitions also increase slightly in the low temperature region, it is assumed that Ln^{3+} and Bi^{3+} ions can also directly absorb intrinsic luminescence, as indicated by arrows 6a and 6b. The energy flow of the UV intrinsic luminescence (arrows 5a and 5b) is very large in $\text{Y}_2\text{O}_3:\text{Eu}^{3+}$ at low temperatures; we assume that this is also the case in $\text{Y}_2\text{O}_3:\text{Tb}^{3+}$, $\text{Y}_2\text{O}_3:\text{Er}^{3+}$ and $\text{Y}_2\text{O}_3:\text{Tm}^{3+}$.

The efficiency of the FRET-mechanism, represented by arrow 4 depends, among other parameters, strongly on the overlap between the spectra of the donor and acceptor states. A simple approximation of this overlap can be obtained by determining the energy difference between the donor and acceptor states: the smaller the energy difference, the larger the overlap and consequently, the larger the energy transfer. In the diagram of Fig. 13 we have indicated the energy levels of the relevant states of Ln^{3+} and Bi^{3+} that will be in resonance with STE-T (and STE-S). These energy levels were taken from Dieke's diagram,³⁰ Table 1 in the publication of Gruber *et al.* for $\text{Y}_2\text{O}_3:\text{Er}^{3+}$ (ref. 19) and from Boulon's data on $\text{Y}_2\text{O}_3:\text{Bi}^{3+}$.²⁰ It can be concluded from Fig. 13 that the spectral overlap between the intrinsic luminescence state (STE-T) with an energy of $28\,300 \text{ cm}^{-1}$ and the $^5\text{D}_2$ state of Tb^{3+} with an energy of about $28\,100 \text{ cm}^{-1}$ must be substantial:

larger than the interactions with the nearby states of Er^{3+} , Tm^{3+} and Bi^{3+} . This qualitative consideration agrees favourably with our experimental evidence. The intrinsic luminescence of Y_2O_3 in $\text{Y}_2\text{O}_3:0.3\% \text{ Tb}^{3+}$ is modest in the 0.3% material and completely absent in the 1% material, whereas it is still substantial in $\text{Y}_2\text{O}_3:1\% \text{ Er}^{3+}$, $\text{Y}_2\text{O}_3:2\% \text{ Tm}^{3+}$, $\text{Y}_2\text{O}_3:1\% \text{ Bi}^{3+}$ and $\text{Y}_2\text{O}_3:0.5\% \text{ Eu}^{3+}$,¹ which have higher concentrations of dopants. The above consideration also agrees with the results of Jacobsohn *et al.*,³ who reported complete quenching of the intrinsic luminescence in $\text{Y}_2\text{O}_3:\text{Tb}^{3+}$ at a doping level of 0.08% (at room temperature and X-ray excitation). In the case of Bi^{3+} the energy difference between the STE-T and the C_{31} levels, which is $28\,300 - 26\,780 = 1520 \text{ cm}^{-1}$,²⁰ is substantial. This is not favourable for effective FRET and it explains why the intrinsic luminescence in $\text{Y}_2\text{O}_3:1\% \text{ Bi}^{3+}$ is rather strong. The FRET mechanism (arrow 4) is very fast and the subsequent radiationless conversion to lower energy levels in Ln^{3+} (not represented in Fig. 13), indicated by arrow 7, is fast as well. The decay from the $\text{Bi}^{3+} \text{C}_{31}$ state to the ground state is $0.6 \mu\text{s}$ at room temperature and increases to about $2 \mu\text{s}$ at $-170 \text{ }^\circ\text{C}$.²⁰ This is still fast enough to maintain the energy transfer via the arrows 4 and 7.

4f–4f energy transfer in $\text{Y}_2\text{O}_3:\text{Er}^{3+}$

The 4f–4f energy transfer in $\text{Y}_2\text{O}_3:\text{Er}^{3+}$ has been studied extensively in our laboratories by laser-activated spectroscopy.^{26,31} The most obvious transfer is from the $^4\text{S}_{3/2}$ state of Er^{3+} to the $^2\text{H}_{11/2}$ state, which causes the spectral radiance of the $^2\text{H}_{11/2} \rightarrow ^4\text{I}_{15/2}$ transition manifold to be substantially temperature-dependent: this can clearly be observed in Fig. 4. Because of this temperature dependency, this manifold is called hot band.³¹ For an accurate analysis of the temperature behaviour of this hot band of $\text{Y}_2\text{O}_3:\text{Er}^{3+}$, the radiance of a transition is a better criterion than SR, because of the variation of the FWHM as a function of temperature.²⁶ Via deconvolution the radiance of transitions can be determined.

Fig. 14 presents the deconvolution of the 539 nm doublet, which is the transition with the largest wavelength of the $^2\text{H}_{11/2} \rightarrow ^4\text{I}_{15/2}$ multiplet.

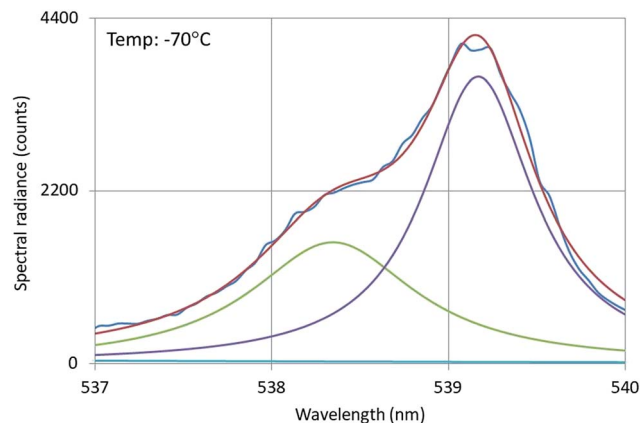


Fig. 14 Deconvolution of the 539 nm doublet of $\text{Y}_2\text{O}_3:\text{Er}^{3+}$. Recorded with a defocused e-beam at 200 kV. Deconvolution with two Lorentzian profiles and least squares fitting to the experimental SR.



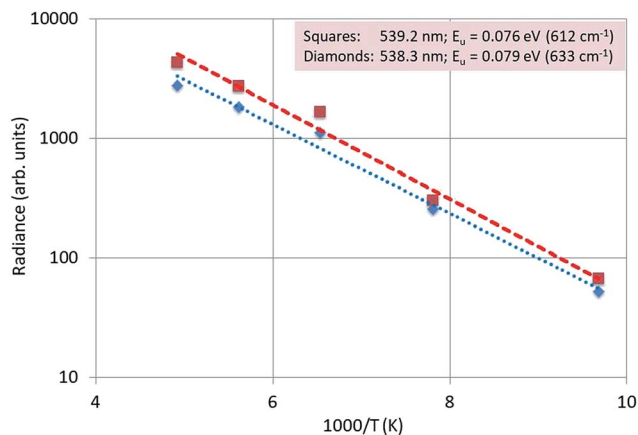


Fig. 15 Arrhenius plot of the radiance of the 539.2 nm and 538.3 nm peaks of $\text{Y}_2\text{O}_3:\text{Er}^{3+}$.

Fig. 15 is an Arrhenius plot of the radiance of the 539.2 nm and 538.3 nm peaks. The dotted and dashed lines were fitted to the experimental points with eqn (1); in this case there was no quenching, because the temperatures were not high enough to observe any quenching of the luminescence.

We found that the average activation energy for this doublet is 0.078 eV (623 cm^{-1}), which is in good agreement with the value (0.08 eV (650 cm^{-1})) determined from the laser-activated spectra.²⁶

Conclusion

CL-spectroscopy at 200 kV in a TEM has been combined in this study with scintillation research, which usually applies to other types of high-energy excitation sources such as X-rays, γ -rays and α -rays. In the present study we have applied a non-focussed e-beam (TEM-mode) at the sample to avoid e-beam degradation. In this case a rather large area of the sample is excited which impedes the collection of CL-spectra from individual nano-sized particles (using a focussed e-beam). With the defocussed e-beam it is possible to study temperature effects with CL-spectroscopy.

The panchromatic images of the $\text{Y}_2\text{O}_3:\text{Ln}^{3+}$ (Ln = Tb, Er and Tm) particles are evidence for uniform doping both in the single particles and also in all particles; this is again a vindication of the synthetic procedure, and ensures that we may trust that all the particles in each sample have the same luminous properties. This is important to allow trust in the CL-data, which lead to the main conclusions of this work. The uniformity of the CL from $\text{Y}_2\text{O}_3:\text{Bi}^{3+}$ particles is less convincing and may indicate that there is some enrichment of Bi^{3+} at the surface of the particles; however, if this is the case, it does not affect the conclusions that can be drawn from this work. More measurements will be necessary to investigate this possible non-uniformity of Bi^{3+} in Y_2O_3 in detail.

In this study we have shown that $\text{Y}_2\text{O}_3:\text{Ln}^{3+}$ (Ln = Tb, Er and Tm) and $\text{Y}_2\text{O}_3:\text{Bi}^{3+}$ show intrinsic luminescence at low temperature and excitation with 200 keV electrons. From Arrhenius-type analyses of the spectral transitions we have

constructed an energy model that describes in detail the energy transfer from the self-trapped excitons to the Ln^{3+} levels. This model also shows why the quenching of the intrinsic luminescence in Y_2O_3 is more effective upon doping with Tb than doping with the other Ln^{3+} ions, due to Förster's resonance energy transfer mechanism.

From the temperature analyses of the CL-spectra of $\text{Y}_2\text{O}_3:\text{Bi}^{3+}$ we could conclude that energy is transferred from Bi^{3+} ions at C_{3i} sites to Bi^{3+} ions at C_2 sites upon increasing the temperature. Until now, this type of energy transfer has been observed only in Y_2O_3 and Lu_2O_3 doped with the lanthanide ions such as Eu^{3+} and Tb^{3+} .^{13,22,23,32} In 2006 Kravchenko *et al.*³³ measured the magnetic properties of bismuth(III) oxy compounds and concluded that Bi_2O_3 is paramagnetic, which indicates that Bi^{3+} must have an unpaired electron in oxy compounds. This brings Bi^{3+} closer to the lanthanide family and makes its energy transfer from the centrosymmetric site to the non-symmetric site more obvious, but still far from clear. Analysis of the CL-spectra of the $^2\text{H}_{11/2} \rightarrow ^4\text{I}_{15/2}$ transition manifold of $\text{Y}_2\text{O}_3:\text{Er}^{3+}$ provided an accurate value of the activation energy that describes its temperature behaviour.

Conflicts of interest

There are no conflicts of interest to declare.

Acknowledgements

We are grateful to the EPSRC and Technology Strategy Board (TSB) for funding the PURPOSE (TP11/MFE/6/1/AA129F; EP-SRC TS/G000271/1) and CONVERTED (JeS no. TS/1003053/1), PRISM (EP/N508974/1) and FAB3D programs. We are finally grateful to the TSB for funding the CONVERT program.

References

- D. den Engelsen, G. R. Fern, T. G. Ireland, P. G. Harris, P. R. Hobson, A. Lipman, R. Dhillon, P. J. Marsh and J. Silver, *J. Mater. Chem. C*, 2016, **4**, 7026–7034.
- A. Fukabori, L. An, A. Ito, V. Chani, K. Kamada, A. Yoshikawa, T. Ikegami and T. Goto, *Ceram. Int.*, 2012, **38**, 2119–2123.
- L. G. Jacobsohn, B. L. Bennett, R. E. Muenchausen, J. F. Smith and D. W. Cooke, *Proc. SPIE*, 2006, **6321**, 63210J.
- R. L. Wood and W. Hayes, *J. Phys. C: Solid State Phys.*, 1982, **15**, 7209–7214.
- T. C. de Oliveira, M. Souza da Silva, L. Menezes de Jesus, D. Vieira Sampaio, J. C. Alves dos Santos, N. R. da Silva Souza and R. Santos da Silva, *Ceram. Int.*, 2014, **40**, 16209–16212.
- G. Blasse and L. H. Brixner, *Eur. J. Solid State Inorg. Chem.*, 1991, **28**, 767–771.
- W. Hayes, M. J. Kane, O. Salminen and A. I. Kuznetsov, *J. Phys. C: Solid State Phys.*, 1984, **17**, L383–L387.
- A. Fukabori, V. Chani, J. Pejchal, K. Kamada, A. Yoshikawa and T. Ikega, *Opt. Mater.*, 2011, **34**, 452–456.
- Y. Fujimoto, T. Yanagida, Y. Yokota, A. Ikesue and A. Yoshikawa, *Opt. Mater.*, 2011, **34**, 448–451.



- 10 K. A. Wickersheim and R. A. Lefever, *J. Electrochem. Soc.*, 1964, **111**, 47–51.
- 11 P. A. Tanner, L. Fu and B. M. Cheng, *J. Phys. Chem. C*, 2009, **113**, 10773–10779.
- 12 T. Förster, *Ann. Phys.*, 1948, **2**, 55–75.
- 13 D. den Engelsen, P. G. Harris, T. G. Ireland and J. Silver, *ECS J. Solid State Sci. Technol.*, 2015, **4**, R1–R9.
- 14 D. den Engelsen, P. G. Harris, T. G. Ireland, R. Withnall and J. Silver, *ECS J. Solid State Sci. Technol.*, 2013, **2**, R201–R207.
- 15 X. Jing, T. Ireland, C. Gibbons, D. J. Barber, J. Silver, A. Vecht, G. Fern, P. Trogwa and D. C. Morton, *J. Electrochem. Soc.*, 1999, **146**, 4654–4658.
- 16 J. Silver, T. G. Ireland and R. Withnall, *J. Electrochem. Soc.*, 2004, **151**, H66–H68.
- 17 D. den Engelsen, P. G. Harris, T. G. Ireland, G. R. Fern and J. Silver, *Ultramicroscopy*, 2015, **157**, 27–34.
- 18 R. P. Leavitt, J. B. Gruber, N. C. Chang and C. A. Morrison, *J. Chem. Phys.*, 1982, **76**, 4775–4788.
- 19 J. B. Gruber, G. W. Burdick, S. Chandra and D. K. Sardar, *J. Appl. Phys.*, 2010, **108**, 023109.
- 20 G. Boulon, *J. Phys.*, 1971, **32**, 333–347.
- 21 R. M. Jafer, E. Coetsee, A. Yousif, R. E. Kroon, O. M. Ntwaeaborwa and H. C. Swart, *Appl. Surf. Sci.*, 2015, **332**, 198–204.
- 22 D. den Engelsen, P. G. Harris, T. G. Ireland, G. Fern and J. Silver, *ECS J. Solid State Sci. Technol.*, 2015, **4**, R145–R152.
- 23 D. den Engelsen, P. G. Harris, T. G. Ireland, G. Fern and J. Silver, *ECS J. Solid State Sci. Technol.*, 2015, **4**, R105–R113.
- 24 F. Baur, F. Glocker and T. Jüstel, *J. Mater. Chem. C*, 2015, **3**, 2054–2064.
- 25 J. Ueda, P. Dorenbos, A. J. J. Bos, A. Meijerink and S. Tanabe, *J. Phys. Chem. C*, 2015, **119**, 25003–25008.
- 26 D. den Engelsen, G. R. Fern, T. Ireland and J. Silver, *J. Lumin.*, submitted.
- 27 J. Silver, M. I. Martinez-Rubio, T. G. Ireland, G. R. Fern and R. Withnall, *J. Phys. Chem.*, 2003, **107**, 1548–1553.
- 28 A. Fukabori, T. Yanagida, J. Pejchal, S. Maeo, Y. Yokota, A. Yoshikawa, T. Ikegami, F. Moretti and K. Kamada, *J. Appl. Phys.*, 2010, **107**, 073501.
- 29 A. Fukabori, V. Chani, K. Kamada, T. Yanagida, Y. Yokota, F. Moretti, N. Kawaguchi and A. Yoshikawa, *J. Cryst. Growth*, 2011, **318**, 823–827.
- 30 G. H. Dieke, *Spectra and Energy Levels of rare Earth Ions in Crystals*, Interscience, 1968.
- 31 J. Silver, M. I. Martinez-Rubio, T. G. Ireland, G. R. Fern and R. Withnall, *J. Phys. Chem. B*, 2001, **105**, 948–953.
- 32 E. Zych, *J. Phys.: Condens. Matter*, 2002, **14**, 5637–5650.
- 33 E. A. Kravchenko, V. G. Orlov and M. P. Shlykov, *Russ. Chem. Rev.*, 2006, **75**, 77–93.

